

# Potential Regulation for Stable Electrocatalysts in Alkaline Water Electrolyzers during Dynamic On and Off Operation through Double-Layer Capacitance Engineering

Published as part of *The Journal of Physical Chemistry C special issue "Degradation of Electrochemical Materials in Energy Conversion and Storage"*.

Tengisbold Gankhuyag, Keisuke Obata, and Kazuhiro Takanabe\*



Cite This: *J. Phys. Chem. C* 2025, 129, 18043–18050



Read Online

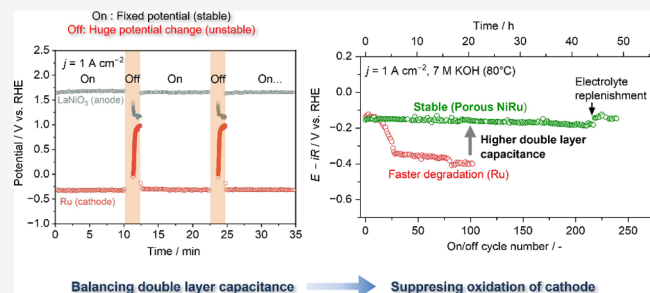
ACCESS |

Metrics & More

Article Recommendations

Supporting Information

**ABSTRACT:** This study explores the impact of reverse current on catalyst degradation in alkaline water electrolysis (AWE) systems that are powered by renewable energy sources (RESs). AWE is a promising technology for green hydrogen generation, but frequent on/off cycling due to RES intermittency poses challenges, including catalyst degradation. This research focuses on two key electrocatalysts: Ru for the hydrogen evolution reaction and LaNiO<sub>3</sub> for the oxygen evolution reaction. The stability of the catalysts was investigated under dynamic operating conditions. The experiments reveal that the redox capacitance is discharged under closed-circuit conditions, which generates a substantial shift of the applied potential in the reverse direction in both the cathode and anode. As a result, reverse current flows and affects the catalyst stability. The Ru cathode degradation was studied with anodes of varying double-layer capacitance ( $C_{dl}$ ). Porous NiRu cathodes with higher  $C_{dl}$  values showed better balance with LaNiO<sub>3</sub> anode, which reduced the changes in the resultant reaching electrode potential and thus mitigated degradation due to dissolution of Ru species. This study provides valuable insights for the design of stable electrode materials for AWE systems that operate under fluctuating conditions and emphasizes the importance of tuning the anode–cathode capacitance ratios to enhance durability and efficiency.



## INTRODUCTION

Hydrogen is widely recognized as a key energy carrier for a future carbon-neutral society due to its high calorific value, zero carbon production, and versatile applications, such as the transportation sector, chemical industry, and heat and power generation for households and industry.<sup>1,2</sup> Green hydrogen generation via water electrolysis using renewable energy sources (RESs) is particularly promising due to its zero carbon footprint.<sup>3</sup> Alkaline water electrolysis (AWE) is the most mature water electrolysis technology and offers the advantage of using non-noble materials such as nickel and iron as catalysts, which contributes to its lower cost.<sup>4,5</sup> AWE has demonstrated potential to achieve good electrochemical performance (2 A cm<sup>-2</sup> at cell voltage <2 V) by minimizing Ohmic losses through efficient bubble evacuation and use of high-activity catalysts.<sup>6–8</sup>

Extensive research has focused on enhancing the current density, but the stability of the RES-powered AWE is still an issue. A significant challenge is catalyst degradation due to frequent on/off (startup/shutdown) cycling of the electrolyzer, which is impeding the widespread use of RES-powered AWE. This cyclic operation is necessary for safety, as the electrolyzer

system must be shut down to prevent explosion if the H<sub>2</sub> concentration in O<sub>2</sub> reaches 2 vol %.<sup>9–11</sup> When using porous diaphragms such as commercial Zirfon, hydrogen impurities in the oxygen increase during low-current-density operation, which limits the reduced operation under partial load of the electrolyzer to 25–40% of its full load.<sup>12–14</sup>

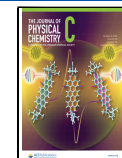
In a typical industrial AWE electrolyzer stack, multiple cells are connected in series through a metallic bipolar plate, and the cathode and anode are polarized due to external electromotive force during electrolysis (Figure 1a). In this bipolar configuration, the cathode and anode of adjacent cells are connected electrically through the bipolar plate as well as ionically through the electrolyte manifold and diaphragms at the same time, making a closed circuit. Thus, a spontaneous

Received: July 6, 2025

Revised: September 12, 2025

Accepted: September 16, 2025

Published: September 25, 2025



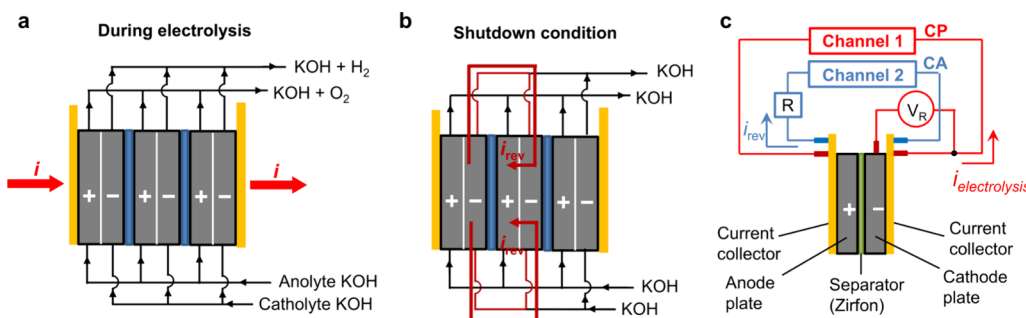


**Figure 1.** (a) Industrial AWE stack during electrolysis. (b) Flow of reverse current upon shutdown in an industrial AWE stack. (c) Experimental single-cell setup that mimics a cell stack, which was used to perform electrolysis ( $i_{\text{electrolysis}}$ ) and measure the reverse current ( $i_{\text{rev}}$ ).

self-discharge process is initiated upon shutdown to close the potential difference between the anode and cathode, which generates a reverse current. Reverse current with the opposite direction to that of the electrolysis current flows through the closed circuit until the anode and cathode reach the same rest potential (Figure 1b). The reverse current induces an unfavorable reduction of the anode catalyst and oxidation of the cathode catalyst, which accelerates their degradation. Therefore, it is necessary to consider this on/off cycling effect on catalyst degradation in long-term stability evaluations under potentiostatic or galvanostatic conditions.<sup>15,16</sup>

Haleem et al. studied the effect of operating parameters such as the current density, temperature, and electrolyte flow rate on the reverse current in a four-cell stack configuration. Their experiment showed that rapid cooling of the cell and stopping the electrolyte flow immediately after shutdown can reduce the overall reverse current. Furthermore, if the anode has a larger charge capacity than the cathode on the same bipolar plate, the cathode is subject to more stress, which makes it more susceptible to corrosion.<sup>17</sup> Oda et al. investigated the discharge behavior of metal oxide-based electrocatalysts and found that the discharge capacity of an electrocatalyst, which should reflect the amount of reverse current during shutdown, is proportional to its Brunauer–Emmett–Teller (BET) surface area.<sup>18</sup>

Nickel mesh electrodes were employed in a two-cell stack, and the nickel mesh on the cathode side was oxidized, while that of the anode side was reduced during reverse current. The major redox couple during the reverse current was assigned to  $\text{NiO}_2/\text{NiOOH}$ .<sup>19</sup> The most important insight from these studies is that the anode and cathode materials should be chosen based not only on their activities but also on their charge capacities in order to minimize the degradation resulting from reverse current.

A recent study by Wang et al. showed that the nickel cathode is prone to severe degradation due to irreversible oxidation of nickel to  $\beta$ -nickel hydroxide during shutdown conditions.<sup>20</sup> Kim et al. also found that the Ni cathode is unstable and demonstrated that a Pb coating is effective for preventing the degradation of Ni cathodes under repeated shutdown conditions.<sup>21,22</sup> Although the Pb/Ni electrocatalyst was tolerant of reverse current, Pb is highly toxic to the environment, including humans, animals, and plants.<sup>23</sup> Kim et al. suggest that the impact of anode reduction during reverse current is negligible, but other studies clearly show that oxygen evolution reaction (OER) catalysts are also prone to reverse current and deactivate faster under such conditions than in constant operation conditions. For example, in nickel cobalt-

based OER catalysts, severe deactivation occurs due to detachment of the catalyst from the nickel substrate when reverse current occurs.<sup>24–26</sup>

Many studies employed an accelerated degradation test (ADT), in which the electrocatalyst was subjected to a constant rest potential that is more cathodic than its OER onset potential, which simulated frequent on/off cycles in the AWE powered by intermittent renewable energy. ADTs in a three-electrode system can help to evaluate the durability of electrocatalysts reasonably with much simpler experimental setups. Nevertheless, the combination of the anode and cathode is crucial for stability, so long-term durability tests using an actual complete AWE cell give more valuable insights into catalyst degradation from the perspective of industrial applications. For example, Sha et al. demonstrated intermittent alkaline seawater electrolysis in a complete AWE cell using a NiCoP-based cathode, which demonstrated that phosphate ion formation and a cobalt oxide passivation layer protect nickel during long-term shutdown conditions in a single cell.<sup>27</sup> However, there are still much fewer studies on the long-term stability of catalysts in complete AWE cells under frequent startup-shutdown conditions compared to the conventional three-electrode system, as shown in Table S1.

To address this gap, we investigated the impact of reverse current on the degradation of a Ru electrocatalyst for the hydrogen evolution reaction (HER) and  $\text{LaNiO}_3$  for the OER in a single cell for water splitting. The cell was equipped with a reversible hydrogen electrode (RHE) as a reference electrode (Figure 1c). Ru electrocatalysts show one of the highest HER activities in alkaline conditions,<sup>28–33</sup> but there has been a lack of detailed studies on the stability of Ru-based cathodes under dynamic on/off operating conditions. Thus, long-term stability tests were performed to measure the potentials of both the anode and cathode in each on/off cycle by using a synchronized measurement protocol with dual channels.

By exploring various combinations of anode and cathode materials, we identified that the ratio of the anode and cathode's double-layer capacitances is a crucial parameter that governs the changes in potential upon shutdown. Our findings demonstrate that the Ru cathode can be stabilized by carefully tuning its double-layer capacitance to balance it with that of the  $\text{LaNiO}_3$  anode. This work provides new insights that could be used for constructing active and stable electrodes for AWE under the fluctuating conditions of RESs.

## METHODS

**Chemicals.** Ni foam and Pt wire were purchased from Nilaco Corporation, and Ni felt (NF) was purchased from

Nikko Techno Corporation. Pt/C gas diffusion electrodes with Pt (0.5 mg cm<sup>-2</sup>) were purchased from Chemix. Hg/HgO (1 M NaOH) reference electrodes were purchased from BAS Inc. Other chemicals were purchased with the following purities from Fujifilm-Wako unless otherwise specified: HCl (35–37%), EtOH ( $\geq$ 99.5%), potassium hydroxide (KOH) ( $\geq$ 85%), nickel(II) nitrate hexahydrate [Ni(NO<sub>3</sub>)<sub>2</sub> · 6H<sub>2</sub>O] ( $\geq$ 98.0%), nickel chloride hexahydrate [NiCl<sub>2</sub> · 6H<sub>2</sub>O] ( $\geq$ 98.0%), ammonium chloride (NH<sub>4</sub>Cl) ( $\geq$ 99.5%), lanthanum(III) acetate sesquihydrate [La(CH<sub>3</sub>COO)<sub>3</sub> · 1.5H<sub>2</sub>O] (Thermo Scientific Chemicals, 99.9%), and ruthenium(III) chloride hydrate [RuCl<sub>3</sub> · xH<sub>2</sub>O] (Sigma-Aldrich). All chemicals were used as received. Zirfon Perl UTP 500+ separators were purchased from Agfa and used as the diaphragms.

**Electrodeposition of Ru on Ni Felt.** The NF substrate was sonicated in ethanol, 10 wt % HCl, and ultrapure water for at least 5 min each and dried at room temperature. Electrodeposition was performed using a 15 mL bath of a 10 mM RuCl<sub>3</sub> solution. The NF was used as the working electrode with an area of 1 cm<sup>2</sup> immersed in the solution, and a carbon rod was used as the counter electrode. Ru was electrodeposited on the NF at a constant current density of  $-100\text{ mA cm}^{-2}$  for 6 min to obtain the Ru/NF electrode.

**Synthesis of LaNiO<sub>3</sub>.** LaNiO<sub>3</sub> was synthesized using a previous protocol reported by Tsukada et al.<sup>34</sup> NF (2.0 cm × 8.0 cm) was washed with acetone, 10% HCl, and ultrapure water under sonication for 5 min each. An aqueous solution containing 0.2 M La(CH<sub>3</sub>COO)<sub>3</sub> · 1.5H<sub>2</sub>O and 0.2 M Ni-(NO<sub>3</sub>)<sub>2</sub> · 6H<sub>2</sub>O was used as a precursor solution. The NF was dipped into the precursor solution for 1 min, followed by calcination in air at 600 °C for 10 min. This process was repeated 16 times before a final calcination in air at 600 °C for 1 h to obtain the LaNiO<sub>3</sub>/NF electrode.

**Synthesis of Porous Ni and Porous NiRu.** Porous Ni was synthesized by dynamic hydrogen bubble-template electrodeposition, which can form a porous structure using H<sub>2</sub> bubbles that are generated during the electrodeposition process.<sup>44,45</sup> NF substrate was used as a working electrode after sonication in ethanol, 10% HCl, and water for 5 min each. The electrodeposition solution contained 0.20 M NiCl<sub>2</sub> and 2.0 M NH<sub>4</sub>Cl. The porous Ni electrocatalyst was electrodeposited at a high current density of  $-1\text{ A cm}^{-2}$  for 10 min (chronopotentiometry (CP)) to obtain porous Ni/NF.<sup>46</sup> For the NiRu electrocatalyst, the electrodeposition solution contained 0.10 M NiCl<sub>2</sub>, 2.0 M NH<sub>4</sub>Cl, and 0.01 M RuCl<sub>3</sub>. The electrodeposition was carried out by applying 8 cycles of  $-1\text{ A cm}^{-2}$  for 1 min and  $100\text{ mA cm}^{-2}$  for 30 s. A carbon rod was used as the counter electrode in each case. This process was used to obtain the porous RuNi/NF electrode.<sup>46</sup>

**Characterization.** X-ray photoelectron spectroscopy (XPS) measurements were conducted with a JEOL JPS-9030 using an Al anode at 300 W, 12 kV, and 25 mA. All acquired data were calibrated using C 1s at 284.6 eV. Inductively coupled plasma optical emission spectroscopy (ICP-OES) measurements were conducted with the Thermo iCAP PRO series. Scanning electron microscopy (SEM) images were obtained with a JEOL JSM IT-800. X-ray diffraction (XRD) patterns were recorded with a Rigaku MiniFlex X-ray diffractometer. Operando Raman spectra were recorded with a Jasco RMP-510 and a CCD camera. The excitation wavelength was 532.048 nm. The working electrode (LaNiO<sub>3</sub>/NF) was immersed in 7 M KOH electrolyte at room temperature for operando Raman spectra measurement.

Platinum wire and Hg/HgO (1 M NaOH) were also immersed in the electrolyte as a counter electrode and reference electrode. The LaNiO<sub>3</sub>/NF working electrode was first activated by applying 1 A cm<sup>-2</sup> for 1 h in 7 M KOH at 353 K before Raman spectroscopy measurements.

**Electrochemical Tests in a Conventional Three-Electrode System.** All electrochemical measurements were carried out using a 16-channel research-grade potentiostat system (VMP3; BioLogic Science Instruments). A polymethylpentene cell with high alkalinity tolerance (BAS Inc.) and a three-electrode configuration was immersed in an aluminum bead bath to keep the electrolyte temperature at 80 °C. O<sub>2</sub> and H<sub>2</sub> were supplied for the OER and HER measurements, while Ar gas was used during double-layer capacitance (C<sub>dl</sub>) measurements. All working electrodes were sealed with poly(tetrafluoroethylene) (PTFE) tape to secure an effective geometric area of 1 cm<sup>2</sup>. HER and OER polarization curves were obtained by applying a constant current of 1 A, 0.8 A, 0.6 A, 0.4 A, 0.2 A, 0.1 A, and 10 mA for 10 min each in 80 °C 7 M KOH solution. Solution resistance was measured by electrochemical impedance spectroscopy (EIS) in a frequency range of 0.1 Hz–200 kHz. A Pt coil and Ni foam were used as the counter electrode for OER and HER measurements, respectively, while Hg/HgO (1 M NaOH) was used as the reference electrode. The following equation was used to convert the recorded potentials to the RHE scale:

$$E_{\text{RHE}} = E_{\text{meas}} + E^0_{\text{Hg/HgO}} + 0.0591\text{ pH}$$

A value of  $E^0_{\text{Hg/HgO}} + 0.0591\text{ pH}$  was determined through experimental calibration (Figure S1). The calibration was carried out by obtaining the current–potential curve of the Pt coil in H<sub>2</sub>-saturated 7 M KOH solution at 80 °C via scanning cyclic voltammograms at 1 mV s<sup>-1</sup>. The OER overpotential ( $\eta$ ) was calculated according to the following equation

$$\eta = E_{\text{RHE}} - E^0_{\text{H}_2\text{O}}$$

The thermodynamic water splitting potential at 80 °C  $E^0_{\text{H}_2\text{O}}$  was calculated by an empirical equation;<sup>47</sup>

$$E^0_{\text{H}_2\text{O}} = 1.229 - 0.9 \times 10^{-3}(T - 298.15)$$

C<sub>dl</sub> values were evaluated in Ar-purged 7 M KOH solution at 80 °C after HER/OER activity tests. The cyclic voltammetry (CV) scanning range was  $-0.550$  to  $-0.350\text{ V}$  vs Hg/HgO for Ru and porous NiRu electrodes. For the LaNiO<sub>3</sub> electrocatalyst, the CV range was 0.066 to 0.266 V vs Hg/HgO. The scan speeds for the Ru and LaNiO<sub>3</sub> electrodes were 50, 40, 30, 20, 10, and 5 mV s<sup>-1</sup>. For the porous Ni electrode and NF, the CV range was  $-0.130$  to  $0.070\text{ V}$  vs Hg/HgO. Faster scan speeds of 500, 400, 300, 200, 100, and 50 mV s<sup>-1</sup> were chosen for the porous Ni electrode and NF substrates.

**Single-Cell Setup for Reverse Current Measurement and Stability Test.** The single-cell electrolyzer had a geometric area of 1 cm<sup>2</sup> and consisted of a platinum-coated titanium flow plate as the anode and a carbon flow plate with an internal RHE reference electrode as the cathode. The detailed electrode setup is shown in Figure S2. The RHE reference electrode was electrically isolated from the cathode flow plate by a PTFE seal, and H<sub>2</sub> gas was introduced with a flow rate of 5 mL min<sup>-1</sup>.

The Zirfon Perl UTP 500+ diaphragm was cut to a size of 3 × 3 cm to ensure contact between the reference electrode and the diaphragm. Thus, the electrocatalyst and reference

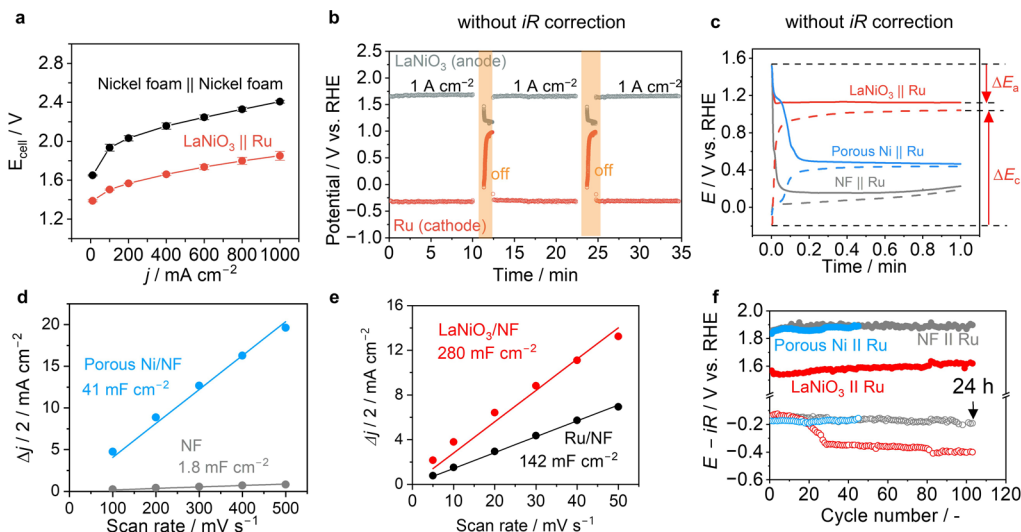


**Figure 2.** (a) Cell voltage at various current densities, (b) potential of cathode and anode upon shutdown, (c) reverse current density upon shutdown, (d, e)  $C_{dl}$  values for various electrodes, and (f) stability test with on/off cycle at  $1 \text{ A cm}^{-2}$  (open symbol: cathode, closed symbol: anode).

electrode were ionically connected through 7 M KOH that had permeated into the diaphragm. The electrolyte tanks and cell were heated to 80 °C, and the temperature behind the reaction field was monitored by a temperature controller with a thermocouple. The 7 M KOH electrolyte was continuously supplied to the anode and cathode flow field from two separate electrolyte tanks at 15 mL min<sup>-1</sup>.

The synchronization protocol for the reverse current measurement is shown in Figure 1d,e. Two channels were connected to the cell at the same time: one was directly connected to the current collector, while a 10-ohm ceramic resistor connected the second channel to the cell. The reverse current through the resistor and cell was measured by using the second channel via chronoamperometry (CA).

## RESULTS

Ru and LaNiO<sub>3</sub> were synthesized, and their HER and OER performance was assessed by CP. The results are shown in Figure S3. The synthesized Ru catalyst required low overpotentials of 32, 59, and 113 mV to deliver current densities of 10, 100, and 1000 mA cm<sup>-2</sup>. The as-synthesized LaNiO<sub>3</sub> catalyst demonstrated excellent OER activity with low overpotentials of 160, 218, and 304 mV to deliver current densities of 10, 100, and 1000 mA cm<sup>-2</sup> in 7 M KOH at 80 °C. Additionally, XRD results of the as-synthesized LaNiO<sub>3</sub> show peaks associated with perovskite LaNiO<sub>3</sub> (Figure S4).

Overall, alkaline water splitting was performed with a single cell using bare nickel foam and the Ru cathode and LaNiO<sub>3</sub> anode. As shown in Figure 2a, the cell voltage was 1.85 V at a high current density of 1 A cm<sup>-2</sup>, which is comparable to state-of-the-art performance in overall AWE. As a comparison, a much higher cell voltage of 2.4 V was observed at 1 A cm<sup>-2</sup> when bare nickel foam was used. The reverse current was investigated using the synchronization protocol (Figure S2d,e). Figure 2b shows the measured potential of the Ru cathode and the LaNiO<sub>3</sub> anode, respectively, during on/off operation. While the potentials of the cathode and anode are constant during normal operation (on condition), their potential drastically changes within just the first 30 s of shutdown (off

condition) and reaches the same rest potential ( $E_{rest} \approx 1.0 \text{ V}_{RHE}$  in this case).

In Figure 2c, the electrode potential upon shutdown is shown when the anode was changed from LaNiO<sub>3</sub> to a porous Ni electrodeposited on NF and bare NF, while the cathode was fixed to Ru. When using the LaNiO<sub>3</sub> anode, the potential of the cathode changed drastically to approximately 1.0 V ( $\Delta E_c$ ), while the potential of the LaNiO<sub>3</sub> anode showed little change ( $\Delta E_a$ ). Surprisingly, the opposite trend was observed when porous Ni and bare NF were used as the anode. The rest potential (where the potentials of the anode and cathode become equal) decreased to around 0.4 and 0.2 V when Ru was combined with these anodes. The reverse current started at approximately 130–140 mA cm<sup>-2</sup> in all cases, but the rate at which it decreased was greatest with the bare NF and slowest with the LaNiO<sub>3</sub> (Figure S5).

We focused on the electrode's double-layer capacitance  $C_{dl}$  to explain this trend because it can be proportional to the total charge accumulation, which leads to the reverse current. As shown in Figure 2d,e,  $C_{dl}$  varied widely between the tested anodes (bare NF: 1.8  $\mu\text{F cm}^{-2}$ , porous Ni: 41  $\mu\text{F cm}^{-2}$ , LaNiO<sub>3</sub>: 286  $\mu\text{F cm}^{-2}$ ), while the Ru cathode's value was maintained (137  $\mu\text{F cm}^{-2}$ ). The potential of the Ru cathode changed drastically when it was combined with LaNiO<sub>3</sub> because the  $C_{dl}$  of LaNiO<sub>3</sub> is almost twice as high as that of Ru. On the other hand,  $\Delta E_c$  was small when using bare NF because it has a much smaller  $C_{dl}$  than Ru.

The stability test with dynamic on and off cycles in a single cell revealed that the Ru cathode activity deteriorated from  $-0.13 \text{ V}_{RHE}$  to  $-0.34 \text{ V}_{RHE}$  in just 30 cycles when combined with LaNiO<sub>3</sub> (Figure 2f). However, it was stable for more than 100 cycles when using bare NF. SEM images of the electrodes from after the stability test show that there was almost no Ru left on the NF substrate when it was combined with LaNiO<sub>3</sub> (Figure S6). The Zirconia separator turned black, which was most likely due to leftover Ru that had adhered to it. When the bare NF anode was used, a uniform layer of Ru was clearly observed on the NF substrate with little detachment after the 24 h stability test.

To gain more insight into the Ru degradation, a stability test was performed with on/off cycles to simulate reverse current using the ADT protocol in a three-electrode system (Figure S7).<sup>32</sup> The ADT protocol involved CP at  $1 \text{ A cm}^{-2}$  for 10 min (on condition), followed by solution-resistance measurement by EIS. Linear sweep voltammetry (LSV) was then performed at  $100 \text{ mV s}^{-1}$  toward the respective resting potentials ( $E_{\text{rest}}$ ) to simulate power fluctuations, after which the potential was held for 1 min during CA to emulate reverse current conditions. Significant Ru degradation was observed when  $E_{\text{rest}}$  was higher than  $1.0 \text{ V}$ , which was similar to the degradation observed in a single cell (Figure 3a). The reverse current was almost twice as

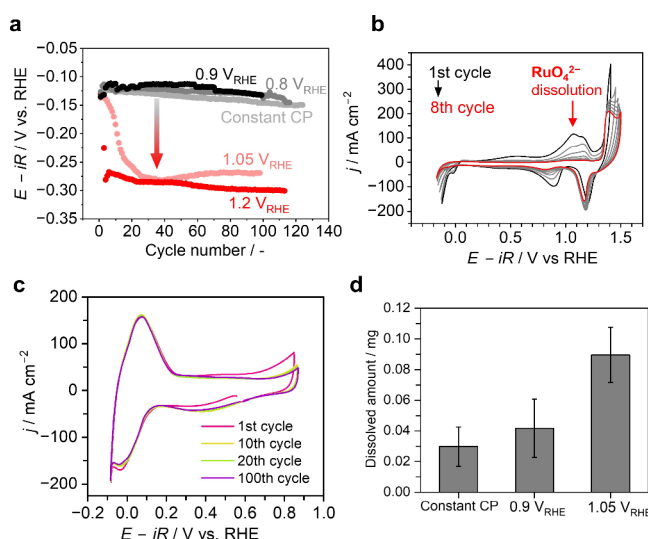
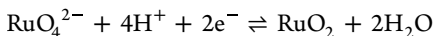


**Figure 3.** (a) Stability test of Ru cathode in 7 M KOH at  $80 \text{ }^\circ\text{C}$  with various rest potentials  $E_{\text{rest}}$ . CV of Ru in Ar-purged 7 M KOH at  $80 \text{ }^\circ\text{C}$  with the range between (b)  $-0.1$  and  $1.41 \text{ V}_{\text{RHE}}$  and (c)  $-0.1$  and  $0.9 \text{ V}_{\text{RHE}}$ , respectively, and (d) amount of Ru dissolved in the electrolyte after 24 h stability test after CV with various  $E_{\text{rest}}$ .

large at  $E_{\text{rest}} = 1.05 \text{ V}_{\text{RHE}}$  as that at  $E_{\text{rest}} = 0.9 \text{ V}_{\text{RHE}}$  (Figure S7b,c). At  $E_{\text{rest}} = 1.05 \text{ V}_{\text{RHE}}$ , the initial reverse current decreased from  $140 \text{ mA cm}^{-2}$  (first cycle) to  $35 \text{ mA cm}^{-2}$  (100th cycle). In contrast, the initial reverse current was almost constant at  $85 \text{ mA cm}^{-2}$  for 100 cycles. The discharge was calculated by integrating the reverse current over time, as shown in Figure S7f. The discharge became smaller as the cycle number increased, which indicated a decrease in the amount of catalysts on the electrode surface. To gain more information about the degradation behavior, CV was performed with Ru in 7 M KOH at  $80 \text{ }^\circ\text{C}$  with 8 repeated scans between  $-0.1 \text{ V}_{\text{RHE}}$  and  $+1.41 \text{ V}_{\text{RHE}}$  (Figure 3b). During the first cycle, a large oxidation peak appears at about  $1.0 \text{ V}_{\text{RHE}}$ , which indicates the oxidation of  $\text{Ru}^{4+}$  to  $\text{Ru}^{6+}$ . This corresponds to the formation of ruthenate ( $\text{RuO}_4^{2-}$ ), which is soluble in an alkaline solution.<sup>35–37</sup>



However, during OER at higher potentials, further oxidation might occur and produce highly oxidized Ru species ( $>6+$ ), which is not stable in an alkaline solution.<sup>36,37</sup> As shown in Figure 3b, the redox peaks of the Ru species decreased significantly as the cycle number increased, which indicated corrosion of the Ru layer on the Ni substrate. Holmin et al. also showed that anodic polarization after HER causes

oxidation of  $\text{RuO}(\text{OH})_2$  into  $\text{RuO}^{2-}$ .<sup>38</sup> Interestingly, the Ru electrode was stable for 100 cycles when CV was performed with a narrower range from  $-0.1 \text{ V}_{\text{RHE}}$  to  $+0.9 \text{ V}_{\text{RHE}}$  (Figure 3c).

The ICP results of the electrolytes after 24 h of dynamic stability testing showed a 3 times higher ruthenium dissolution at  $E_{\text{rest}} = 1.05 \text{ V}_{\text{RHE}}$  compared to the cases of constant CP and  $E_{\text{rest}} = 0.9 \text{ V}_{\text{RHE}}$  (Figure 3d). This result further indicates that the Ru electrode is not stable if its potential becomes higher than  $1.0 \text{ V}_{\text{RHE}}$  because it oxidizes into ruthenate species and dissolves in the alkaline electrolyte. Notable agglomerations and exposed nickel surfaces were observed in the SEM image obtained after the stability test at  $E_{\text{rest}} = 1.05 \text{ V}_{\text{RHE}}$  (Figure S8). XPS was employed to gain insight into the surface electronic structure of Ru after applying  $0.9 \text{ V}_{\text{RHE}}$  and  $1.2 \text{ V}_{\text{RHE}}$  (Figure S9). The Ru 3p peak indicates the presence of almost metallic Ru after application of  $0.9 \text{ V}_{\text{RHE}}$ . In contrast, the Ru 3p peak shifted to higher binding energy and became more like the  $\text{RuO}_2$  peak after applying  $1.2 \text{ V}_{\text{RHE}}$ .<sup>48</sup>

The effects of  $E_{\text{rest}}$  were also investigated in a three-electrode system with a  $\text{LaNiO}_3$  electrode (Figures 4 and S7). The same

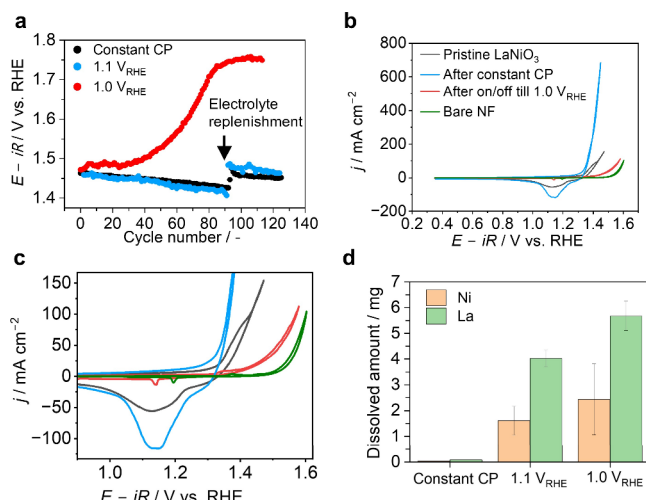


**Figure 4.** (a) Stability test of  $\text{LaNiO}_3/\text{NF}$  with various rest potentials  $E_{\text{rest}}$ . (b) CV of  $\text{LaNiO}_3$  and bare NF in Ar-purged 7 M KOH in  $80 \text{ }^\circ\text{C}$ , where (c) is enlarged figure of (b), and (d) amount of Ni and La dissolved in the electrolyte after the 24 h stability test.

ADT protocol was used (Figure S7a). The  $\text{LaNiO}_3$  electrode was stable in the constant-CP stability test, and when  $E_{\text{rest}}$  was  $1.1 \text{ V}_{\text{RHE}}$ , but significant deactivation was observed when  $E_{\text{rest}}$  was  $1.0 \text{ V}_{\text{RHE}}$ . The reverse current was almost twice as large at  $E_{\text{rest}} = 1.0 \text{ V}_{\text{RHE}}$  as that at  $E_{\text{rest}} = 1.1 \text{ V}_{\text{RHE}}$  (Figure S7d,e). At  $E_{\text{rest}} = 1.0 \text{ V}_{\text{RHE}}$  the initial reverse current decreased from over  $400 \text{ mA cm}^{-2}$  (first cycle) to less than  $30 \text{ mA cm}^{-2}$  (100th cycle). CV was performed for each electrode after 24 h of dynamic stability testing, as shown in Figure 4b,c. Redox peaks near  $1.15 \text{ V}_{\text{RHE}}$  and  $1.4 \text{ V}_{\text{RHE}}$  were observed for every sample and were assigned to the  $\text{NiOOH}/\text{Ni(OH)}_2$  ( $\text{Ni}^{3+}/\text{Ni}^{2+}$ ) redox couple.<sup>39–41</sup> The  $\text{LaNiO}_3$  electrode demonstrated a much larger reduction peak than the pristine  $\text{LaNiO}_3$  electrode after the 24 h stability test because of catalyst activation at anodic OER potential, which was most likely due to the well-known surface reconstruction of perovskite for OER.<sup>42</sup>

After on/off cycling at  $E_{\text{rest}} = 1.0 \text{ V}_{\text{RHE}}$ , the  $\text{LaNiO}_3$  electrode showed a small reduction peak that was almost identical to that

of bare NF. This indicates that a significant number of catalytic sites of Ni were lost during on/off cycling. The observed deactivation is mostly due to mechanical peeling of  $\text{LaNiO}_3$  from the NF substrate at high current density, as there was a large amount of precipitated black powder in the electrolyte. This is supported by the significant amount of Ni and La found in the ICP analysis of the electrolyte after on/off cycling, as shown in Figure 4d. Lee et al. reported that the incomplete reduction of the OER active phase  $\gamma\text{-NiOOH}$  to  $\beta\text{-Ni(OH)}_2$  results in significant degradation during many redox cycles.<sup>43</sup> Frequent on/off cycling could trigger this irreversible redox if the  $E_{\text{rest}}$  value is as low as 1.0 V and could also induce catalyst peeling due to bubble generation at a high current density. Almost complete peeling of the catalyst layer from the NF substrate was observed in the SEM image obtained after the stability test at  $E_{\text{rest}} = 1.0 \text{ V}_{\text{RHE}}$  (Figure S10). In comparison, more catalyst was present as  $E_{\text{rest}}$  increased to 1.1 V, and needle-like catalyst was distributed uniformly on the electrode after only constant CP. To gain insight into more direct evidence related to the reduction of  $\gamma\text{-NiOOH}$  to  $\beta\text{-Ni(OH)}_2$ , we conducted *in situ* operando Raman spectroscopy measurements in 7 M KOH at room temperature. First, the potential was set to 1.4  $\text{V}_{\text{RHE}}$  for 10 min before 1.1  $\text{V}_{\text{RHE}}$ . Then, the potential was set back to 1.4  $\text{V}_{\text{RHE}}$  for 10 min, after which 1.0  $\text{V}_{\text{RHE}}$  was applied. Two peaks at around 475 and 555  $\text{cm}^{-1}$  were observed at 1.4  $\text{V}_{\text{RHE}}$ , which correspond to the vibration of NiOOH (Figure 5a,b).<sup>49,50</sup> The NiOOH peak intensity

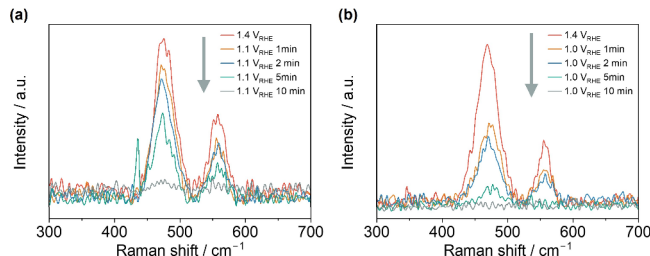


**Figure 5.** Operando Raman spectroscopy of  $\text{LaNiO}_3/\text{NF}$  in 7 M KOH at room temperature. (a) Applied potential of 1.1  $\text{V}_{\text{RHE}}$ . (b) Applied potential of 1.0  $\text{V}_{\text{RHE}}$ .

decreased much faster when 1.0  $\text{V}_{\text{RHE}}$  was applied, and the NiOOH peaks completely disappeared after 10 min. In contrast, a more gradual change was observed when 1.1  $\text{V}_{\text{RHE}}$  was applied, and very small NiOOH peaks were still observable after 10 min. This result suggests that the reduction of  $\gamma\text{-NiOOH}$  to  $\beta\text{-Ni(OH)}_2$  happens much faster when  $E_{\text{rest}}$  equals 1.0  $\text{V}_{\text{RHE}}$ , while it is more gradual when  $E_{\text{rest}}$  equals 1.1  $\text{V}_{\text{RHE}}$ . Thus, rapid  $\text{LaNiO}_3$  degradation was observed when 1.0  $\text{V}_{\text{RHE}}$  was applied during the accelerated stress test.

Then we tested the stability of  $\text{LaNiO}_3 \parallel \text{Ru}$  in a single-cell configuration. It was hypothesized that the Ru cathode could be stabilized if its potential is kept below 1.0 V, which we tested by designing a porous NiRu cathode with a very high double-layer capacitance of  $365 \text{ mF cm}^{-2}$ , comparable to that for  $\text{LaNiO}_3$  (Figure 6a). As shown in Figure 6b, the porous NiRu had excellent stability even after almost 250 on/off cycles for 3 days when combined with the  $\text{LaNiO}_3$  anode. As expected, its potential was successfully maintained below 0.5  $\text{V}_{\text{RHE}}$  upon shutdown, which is below the dissolution threshold due to its higher double-layer capacitance than that of the Ru cathode (Figure 6d). The CV of as-made porous NiRu also shows  $\text{Ru}^{6+}$  formation at around 1.0  $\text{V}_{\text{RHE}}$ , indicating the

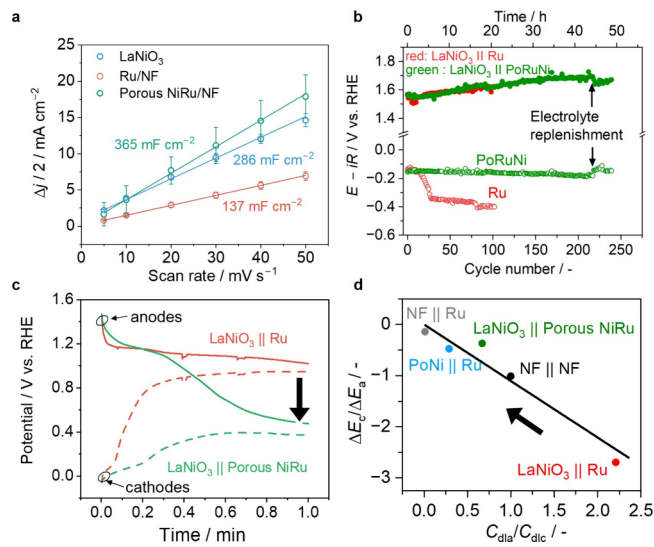


**Figure 6.** (a) Current density associated with  $C_{\text{dl}}$  values as a function of scan rates, (b) stability test of  $\text{LaNiO}_3$  and as-obtained or porous Ni substrate with on/off cycles at  $1 \text{ A cm}^{-2}$ , (c) relationship between the  $C_{\text{dl}}$  ratio and potential change ratio, and (d) potential of anode and cathode measured during shutdown condition.

dissolution of Ru (Figure S11). This suggests that the excellent stability of porous NiRu is due to the regulated rest potential during shutdown conditions, not due to other factors. Regarding the  $\text{LaNiO}_3$  anode, this test did not cause much deactivation, while apparent quicker deactivation was observed in the three-electrode system (Figure 4a). The difference may come from the operation where quick LSV ( $100 \text{ mV s}^{-1}$ ) was conducted to  $E_{\text{rest}}$  right after  $1 \text{ A cm}^{-2}$  CP in the three-electrode system compared to gradual potential relaxation via shutdown operation (open circuit condition). The forced reduction of Ni species in  $\text{LaNiO}_3$  as well as the Ni substrate at  $\sim 1.0 \text{ V}_{\text{RHE}}$  may induce mechanical shock, leading to severe detaching and consequent deactivation. As expected, when the LSV scan rate was lowered to  $10 \text{ mV s}^{-1}$ , the degradation rate of  $\text{LaNiO}_3$  was 3 times lower when compared to  $100 \text{ mV s}^{-1}$  in the three-electrode system (Figure S12).

As discussed previously (Figure 2), the reaching potential of a single cell is strongly influenced by the capacity of the respective electrode substrates in a single-cell configuration. Indeed, a linear correlation was observed between the ratio of potential shifts ( $\Delta E_a/\Delta E_c$  designated in Figure 2c) and  $C_{\text{dl}}$  ratios ( $C_{\text{dlc}}/C_{\text{da}}$ ) (Figure 6d), which confirmed that  $C_{\text{dl}}$  reasonably represents the charge accumulation and resultant resting potential (the subscripts “a” and “c” indicate the anode and the cathode, respectively). An increase in cathode capacitance shifts the reaching potential in the negative direction, whereas an increase in anode capacitance shifts it in the positive direction, reflecting opposite trends. By combining the knowledge of the electrodes’ chemical nature, reverse current behavior with potential control is possible for improved stable performance operation. In this case, chemical dissolution of Ru was avoided by keeping the reaching potential more negative than the dissolution potential. Further investigation is, however, still necessary to improve the strong mechanical binding of an oxide, such as  $\text{LaNiO}_3$ , to the metallic substrate by immense perturbation of the potential sweep. In summary, this study offers novel insights that significantly advance our understanding and control of retrogressive current

behavior and resultant durability upon on and off cycles in the AWE system and beyond.

## CONCLUSIONS

This study characterized the degradation of Ru cathodes and LaNiO<sub>3</sub> anodes for an AWE single cell under reverse current generated during dynamic on/off operation by ADTs. Electrochemical measurements were effectively utilized to compare CV in a conventional three-electrode system to get more insights into each electrode. Our synchronization protocol enabled the investigation of reverse current in a more practical single cell, and the critical role of  $C_{dl}$  in changes in the electrode potential during shutdown was clarified. Balancing the  $C_{dl}$  values of the anode and cathode mitigated unfavorable Ru oxidation, thereby prolonging the cathode's lifespan for AWE operation. As long as the Ru potential remains below its dissolution threshold ( $\sim 1.0$  V<sub>RHE</sub>), stability can be maintained. These findings underscore the critical role of charge capacity matching in preventing degradation from redox imbalance. Adjusting  $C_{dl}$  offers one of the practical means of tuning the resting potential under closed-circuit conditions. The electrolyzer lifetime could be increased based on knowledge of the redox properties for both the cathode and anode and by controlling the rest potential.

## ASSOCIATED CONTENT

### Supporting Information

The Supporting Information is available free of charge at <https://pubs.acs.org/doi/10.1021/acs.jpcc.Sc04643>.

Detailed description of synchronization protocol, photographs of experimental setup, SEM images of electrodes after ADT, and measured reverse current and discharge ([PDF](#))

## AUTHOR INFORMATION

### Corresponding Author

Kazuhiko Takanabe – Department of Chemical System Engineering, School of Engineering, The University of Tokyo, Bunkyo-ku, Tokyo 113-8656, Japan;  [orcid.org/0000-0001-5374-9451](http://orcid.org/0000-0001-5374-9451); Email: [takanabe@chemsys.t.u-tokyo.ac.jp](mailto:takanabe@chemsys.t.u-tokyo.ac.jp)

### Authors

Tengisbold Gankhuyag – Department of Chemical System Engineering, School of Engineering, The University of Tokyo, Bunkyo-ku, Tokyo 113-8656, Japan

Keisuke Obata – Department of Chemical System Engineering, School of Engineering, The University of Tokyo, Bunkyo-ku, Tokyo 113-8656, Japan;  [orcid.org/0000-0003-3544-9505](http://orcid.org/0000-0003-3544-9505)

Complete contact information is available at: <https://pubs.acs.org/10.1021/acs.jpcc.Sc04643>

### Author Contributions

T.G. performed all electrochemical experiments and analyses. All the authors wrote the manuscript, and K.T. obtained the funding and supervised the project.

### Notes

The authors declare no competing financial interest.

## ACKNOWLEDGMENTS

The authors are grateful to the following for their support: GteX Program Japan (Grant Number JPMJGX23H2) and the MEXT Program: Data Creation and Utilization-Type Material Research and Development Project (Grant Number JPMXP1122712807). T.G. acknowledges the scholarship support from Iwatani Naoji Foundation.

## REFERENCES

- (1) International Renewable Energy Agency *World Energy Transitions Outlook: 1.5°C Pathway*; International Renewable Energy Agency, 2021.
- (2) International Energy Agency *Net Zero by 2050: A Roadmap for the Global Energy Sector*; International Energy Agency, 2021.
- (3) Kumar, S. S.; Lim, H. An overview of water electrolysis technologies for green hydrogen production. *Energy Rep.* **2022**, *8*, 13793–13813.
- (4) Sebbahi, S.; Assila, A.; Belghiti, A. A.; Laasri, S.; Kaya, S.; Hlil, E. K.; Rachidi, S.; Hajjaji, A. A comprehensive review of recent advances in alkaline water electrolysis for hydrogen production. *Int. J. Hydrogen Energy* **2024**, *82*, 583–599.
- (5) Brauns, J.; Turek, T. Alkaline Water Electrolysis Powered by Renewable Energy: A Review. *Processes* **2020**, *8*, 248.
- (6) Rocha, F.; Georgiadis, C.; Droogenbroek, K. V.; Delmelle, R.; Pinon, X.; Pyka, G.; Kerckhofs, G.; Egert, F.; Razmjooei, F.; Ansar, S.; Mitsushima, S.; Proost, J. Proton exchange membrane-like alkaline water electrolysis using flow-engineered three-dimensional electrodes. *Nat. Commun.* **2024**, *15*, 7444.
- (7) Li, Z.; Lin, G.; Wang, L.; Lee, H.; Du, J.; Tang, T.; Ding, G.; Ren, R.; Li, W.; Cao, X.; Ding, S.; Ye, W.; Yang, W.; Sun, L. Seed-assisted formation of NiFe anode catalysts for anion exchange membrane water electrolysis at industrial-scale current density. *Nat. Catal.* **2024**, *7*, 944–952.
- (8) Chen, Y.; Li, Q.; Lin, Y.; Liu, J.; Pan, J.; Hu, J.; Xu, X. Boosting oxygen evolution reaction by FeNi hydroxide-organic framework electrocatalyst toward alkaline water electrolyzer. *Nat. Commun.* **2024**, *15*, 7278.
- (9) Haug, P.; Koj, M.; Turek, T. Influence of process conditions on gas purity in alkaline water electrolysis. *Int. J. Hydrg. Energy* **2017**, *42*, 9406–9418.
- (10) Schalenbach, M.; Lueke, W.; Stolten, D. Hydrogen Diffusivity and Electrolyte Permeability of the Zirfon PERL Separator for Alkaline Water Electrolysis. *J. Electrochem. Soc.* **2016**, *163*, F1480–F1488.
- (11) Haoran, C.; Xia, Y.; Wei, W.; Yongzhi, Z.; Bo, Z.; Leiqi, Z. Safety and efficiency problems of hydrogen production from alkaline water electrolyzers driven by renewable energy sources. *Int. J. Hydrogen Energy* **2024**, *54*, 700–712.
- (12) Brauns, J.; Schönebeck, J.; Kraglund, M. R.; Aili, D.; Hnat, J.; Žitka, J.; Mues, W.; Jensen, J. O.; Bouzek, K.; Turek, T. Evaluation of Diaphragms and Membranes as Separators for Alkaline Water Electrolysis. *J. Electrochem. Soc.* **2021**, *168* (1), No. 014510.
- (13) Ursúa, A.; Barrios, E. L.; Pascual, J.; San Martín, I.; Sanchis, P. Integration of commercial alkaline water electrolyzers with renewable energies: limitations and improvements. *Int. J. Hydrogen Energy* **2016**, *41* (30), 12852–12861.
- (14) Lee, B.; Lim, D.; Lee, H.; Lim, H. Which water electrolysis technology is appropriate? Critical insights of potential water electrolysis for green ammonia production. *Renew. Sustain. Energy Rev.* **2021**, *143*, No. 110963.
- (15) Ehlers, J. C.; Feidenhans'l, A. A.; Therkildsen, K. T.; Larrazábal, G. O. Affordable Green Hydrogen from Alkaline Water Electrolysis: Key Research Needs from an Industrial Perspective. *ACS Energy Lett.* **2023**, *8*, 1502–1509.
- (16) Kojima, H.; Nagasawa, K.; Todoroki, N.; Ito, Y.; Matsui, T.; Nakajima, R. Influence of renewable energy power fluctuations on water electrolysis for green hydrogen production. *Int. J. Hydrogen Energy* **2023**, *48*, 4572–4593.

- (17) Haleem, A. A.; Huyan, J.; Nagasawa, K.; Mitsushima, S.; et al. Effects of operation and shutdown parameters and electrode materials on the reverse current phenomenon in alkaline water analyzers. *J. Power Sources* **2022**, *535*, No. 231454.
- (18) Oda, K.; Kuroda, Y.; Mitsushima, S. Investigation of Charge–Discharging Behavior of Metal Oxide-Based Anode Electrocatalysts for Alkaline Water Electrolysis to Suppress Degradation due to Reverse Current. *Electrocatalysis* **2023**, *14*, 499–510.
- (19) Uchino, Y.; Kobayashi, T.; Hasegawa, S.; Nagashima, I.; Sunada, Y.; Manabe, A.; Nishiki, Y.; Mitsushima, S. Relationship Between the Redox Reactions on a Bipolar Plate and Reverse Current After Alkaline Water Electrolysis. *Electrocatalysis* **2018**, *9*, 67–74.
- (20) Wang, G.; Li, H.; Babbe, F.; Tricker, A.; Crumlin, J. E.; Yano, J.; Mukundan, R.; Peng, X. Probing Electrode Transformation under Dynamic Operation for Alkaline Water Electrolysis. *Adv. Energy Mater.* **2025**, *15*, No. 2500886.
- (21) Jung, S. M.; Kim, Y.; Lee, B. J.; Jung, H.; Kwon, J.; Lee, J.; Kim, K. S.; Kim, Y. W.; Kim, K. J.; Cho, H. S.; Park, J. H.; Han, J. W.; Kim, Y. T. Reverse-Current Tolerance for Hydrogen Evolution Reaction Activity of Lead-Decorated Nickel Catalysts in Zero-Gap Alkaline Water Electrolysis Systems. *Adv. Funct. Mater.* **2024**, *34* (27), No. 2316150.
- (22) Kim, Y.; Jung, S.; Kim, K.; Kim, H.; Kwon, J.; Lee, J.; Cho, H.; Kim, Y. Cathodic Protection System against a Reverse-current after Shut-down in Zero-Gap Alkaline Water Electrolysis. *JACS Au* **2022**, *2*, 2491–2500.
- (23) Wani, A. L.; Ara, A.; Usmani, J. A. Lead toxicity: a review. *Interdiscip. Toxicol.* **2015**, *8* (2), 55–64.
- (24) Abdel Haleem, A. A.; Nagasawa, K.; Kuroda, Y.; Nishiki, Y.; Zaenal, A.; Mitsushima, S. A New Accelerated Durability Test Protocol for Water Oxidation Electrocatalysts of Renewable Energy Powered Alkaline Water Electrolyzers. *Electrochemistry* **2021**, *89* (2), 186–191.
- (25) Todoroki, N.; Nagasawa, K.; Enjoji, H.; Mitsushima, S. Suppression of Catalyst Layer Detachment by Interfacial Microstructural Modulation of the  $\text{NiCo}_2\text{O}_4/\text{Ni}$  Oxygen Evolution Electrode for Renewable Energy-Powered Alkaline Water Electrolysis. *ACS Appl. Mater. Interfaces* **2023**, *15*, 24399–24407.
- (26) Kuroda, Y.; Nishimoto, T.; Mitsushima, S. Self-repairing hybrid nanosheet anode catalysts for alkaline water electrolysis connected with fluctuating renewable energy. *Electrochim. Acta* **2019**, *323*, No. 134812.
- (27) Sha, Q.; Wang, S.; Yan, L.; Feng, Y.; Zhang, Z.; Li, S.; Guo, X.; Li, T.; Li, H.; Zhuang, Z.; Zhou, D.; Liu, B.; Sun, X. 10000-h-stable intermittent alkaline seawater electrolysis. *Nature* **2025**, *639*, 360–367.
- (28) Yu, J.; He, Q.-J.; Yang, G. M.; Zhou, W.; Shao, Z. P.; Ni, M. Recent Advances and Prospective in Ruthenium-Based Materials for Electrochemical Water Splitting. *ACS Catal.* **2019**, *9* (11), 9973–10011.
- (29) Yang, Y.; Yu, Y.; Li, J.; Chen, Q.; et al. Engineering Ruthenium-Based Electrocatalysts for Effective Hydrogen Evolution Reaction. *Nano-Micro Lett.* **2021**, *13* (1), 160.
- (30) Zhao, S.; Hung, S.-F.; Deng, L.; Zeng, W.-J.; Xiao, T.; Li, S.; Kuo, C.-H.; Chen, H.-Y.; Hu, F.; Peng, S. Constructing regulable supports via non-stoichiometric engineering to stabilize ruthenium nanoparticles for enhanced pH-universal water splitting. *Nat. Commun.* **2024**, *15*, 2728.
- (31) Zhao, J.; Urrego-Ortiz, R.; Liao, N.; Calle-Vallejo, F.; Luo, J. Rationally designed Ru catalysts supported on TiN for highly efficient and stable hydrogen evolution in alkaline conditions. *Nat. Commun.* **2024**, *15* (1), 6391.
- (32) Zuo, Y.; Bellani, S.; Ferri, M.; Saleh, G.; Shinde, D. V.; Zappia, M. I.; Brescia, R.; Prato, M.; De Trizio, L.; Infante, I.; Bonaccorso, F.; Manna, L. High-performance alkaline water electrolyzers based on Ru-perturbed Cu nanoplatelets cathode. *Nat. Commun.* **2023**, *14*, 4680.
- (33) Yao, R.; Sun, K.; Zhang, K.; Wu, Y.; Du, Y.; et al. Stable hydrogen evolution reaction at high current densities via designing the Ni single atoms and Ru nanoparticles linked by carbon bridges. *Nat. Commun.* **2024**, *15*, 2218.
- (34) Tsukada, Y.; Kuroda, Y.; Niilo, H.; Fujii, Y.; Fujimoto, N.; Mitsushima, S. Measurement of powdery oxygen evolution reaction catalyst under practical current density using pressure-bonded electrodes. *Electrochim. Acta* **2020**, *353*, No. 136544.
- (35) Chalupczok, S.; Kurzweil, P.; Hartmann, H.; Schell, C. The Redox Chemistry of Ruthenium Dioxide: A Cyclic Voltammetry Study—Review and Revision. *Int. J. Electrochem. Sci.* **2018**, *2018*, No. 1273768.
- (36) Bewick, A.; Gutiérrez, C.; Laramona, G. In-situ IR spectroscopy study of the ruthenium electrode in acid and alkaline solutions. *J. Electroanal. Chem.* **1992**, *332* (1–2), 155–167.
- (37) Povar, I.; Spinu, O. Ruthenium redox equilibria: 3. Pourbaix diagrams for the systems  $\text{Ru}-\text{H}_2\text{O}$  and  $\text{Ru}-\text{Cl}-\text{H}_2\text{O}$ . *J. Electrochem. Sci. Eng.* **2016**, *6* (1), 145–153.
- (38) Holmin, S.; Näslund, L.-Å.; Ingason, A. S.; Rosén, J.; Zimmerman, E. Corrosion of ruthenium dioxide based cathodes in alkaline medium caused by reverse currents. *Electrochim. Acta* **2014**, *146*, 30–36.
- (39) Singh, S. P.; Singh, R. N.; Poillevert, G.; Chartier, P. Physicochemical and electrochemical characterization of active films of  $\text{LaNi}_3$  for use as anode in alkaline water electrolysis. *Int. J. Hydrogen Energy* **1995**, *20*, 203–210.
- (40) Hall, D. S.; Bock, C.; MacDougall, B. R. The Electrochemistry of Metallic Nickel: Oxides, Hydroxides, Hydrides and Alkaline Hydrogen Evolution. *J. Electrochem. Soc.* **2013**, *160* (3), F235–F243.
- (41) Lyons, M. E. G.; Doyle, R. L.; Godwin, I.; O'Brien, M.; Russell, L. Hydrous Nickel Oxide: Redox Switching and the Oxygen Evolution Reaction in Aqueous Alkaline Solution. *J. Electrochem. Soc.* **2012**, *159* (11), H932–H937.
- (42) Zhao, J.; Shi, Z.; Li, C.; Ren, Q.; Li, G. Regulation of Perovskite Surface Stability on the Electrocatalysis of Oxygen Evolution Reaction. *ACS Materials Lett.* **2021**, *3* (6), 721–737.
- (43) Lee, S.; Kim, I.; Cho, H.; Kim, C.; Lee, Y. Resolving Potential-Dependent Degradation of Electrodeposited  $\text{Ni}(\text{OH})_2$  Catalysts in Alkaline Oxygen Evolution Reaction (OER): In Situ XANES Studies. *Appl. Catal., B* **2021**, *284*, No. 119729.
- (44) Jiang, H.; Sun, Y.; You, B. Dynamic Electrodeposition on Bubbles: An Effective Strategy toward Porous Electrocatalysts for Green Hydrogen Cycling. *Acc. Chem. Res.* **2023**, *56* (11), 1421–1432.
- (45) Shin, H.; Dong, J.; Liu, M. Nanoporous Structures Prepared by an Electrochemical Deposition Process. *Adv. Mater.* **2003**, *15* (19), 1610–1614.
- (46) Marozzi, C. A.; Chialvo, A. C. Development of electrode morphologies of interest in electrocatalysis. Part I: electrodeposited porous nickel electrodes. *Electrochim. Acta* **2000**, *45* (12), 2111–2120.
- (47) Awasthi, A.; Scott, K.; Basu, S. Dynamic modeling and simulation of a proton exchange membrane electrolyzer for hydrogen production. *Int. J. Hydrogen Energy* **2011**, *36* (22), 14779–14786.
- (48) Morgan, D. J. Resolving ruthenium: XPS studies of common ruthenium materials. *Surf. Interface Anal.* **2015**, *47*, 1072–1079.
- (49) Yeo, B. S.; Bell, A. T. In Situ Raman Study of Nickel Oxide and Gold-Supported Nickel Oxide Catalysts for the Electrochemical Evolution of Oxygen. *J. Phys. Chem. C* **2012**, *116*, 8394–8400.
- (50) Bantignies, J. L.; Deabate, S.; Righi, A.; Rols, S.; Hermet, P.; Sauvajol, J. L.; Henn, F. New Insight into the Vibrational Behavior of Nickel Hydroxide and Oxyhydroxide Using Inelastic Neutron Scattering, Far/Mid-Infrared and Raman Spectroscopies. *J. Phys. Chem. C* **2008**, *112*, 2193–2201.